INTERNATIONAL JOURNAL FOR NUMERICAL METHODS IN FLUIDS
Int. J. Numer. Meth. Fluids 2009; **59**:1321–1349
Published online 17 July 2008 in Wiley InterScience (www.interscience.wiley.com). DOI: 10.1002/fld.1869

Mobility of shear thinning viscous drops in a shear Newtonian carrying flow using DR-BEM

M. Giraldo[1], H. Power[2,*,†] and W. Flórez[1]

[1]*Instituto de Energía y Termodinámica, Universidad Pontificia Bolivariana, Circ. 1 No. 73-34, Medellín, Colombia*
[2]*School of Mechanical, Materials and Manufacturing Engineering, The University of Nottingham, Nottingham NG7 2RD, U.K.*

SUMMARY

The study of drop behaviour has attracted great interest in the last years due to its importance in different industrial and biological systems. Most available works focus on Newtonian drops, excluding some very important applications such as polymer mixing. Simulations of non-Newtonian drops have had only limited study, mostly in time-dependent rheologies or simple flow cases. This work presents a boundary-only formulation based on the dual reciprocity method to model the motion and deformation of non-Newtonian shear thinning drops due to a shear Newtonian unbounded carrying flow. Pair-wise interactions at low Reynolds number between two viscous shear thinning non-Newtonian drops are numerically simulated in order to obtain mobility magnitudes under linear shear flow of different strengths. Separation of the drops in the direction perpendicular to the imposed flow field at high capillary number (small surface tension) and low viscosity ratio was favoured by shear thinning, increasing in magnitude as the capillary number increases and the viscous ratio decreases. Higher values of this separation occur at higher values of the viscosity ratio when compared with the case of Newtonian drops. In order to obtain a good physical description of the non-Newtonian drop behaviour, while maintaining good computational performance, the non-Newtonian viscosity is made to obey the truncated power law model. Copyright © 2008 John Wiley & Sons, Ltd.

Received 28 September 2007; Revised 9 May 2008; Accepted 25 May 2008

KEY WORDS: boundary integral methods; low-Reynolds-number flows; mobility; shear thinning drops

1. INTRODUCTION

Different authors have undertaken the task of studying flows involving the motion and deformation of viscous drops. Some works analyse single drop under different flow conditions, such as [1–3],

*Correspondence to: H. Power, School of Mechanical, Materials and Manufacturing Engineering, The University of Nottingham, Nottingham NG7 2RD, U.K.
†E-mail: henry.power@nottingham.ac.uk

Contract/grant sponsor: COLCIENCIAS

while others study more complex situations such as the interaction of two or more drops or the deformation of drops inside closed domains, see [4–9]. From a modelling perspective, it is important to consider that the flow fields outside and inside the drops behave differently but depending on each other and the properties of the interface, see [8, 10].

The analytical solutions to this type of problems, drops motion and deformation, tend to be complex and possess limited validity; therefore, numerical solutions are the most often chosen form of solution. In this case, conventional numerical methods such as the finite element method [11] or the finite difference method can often be computational costly in this case because the drop surfaces are not fixed but changing in time [12], situation for which these methods require remeshing at each time step or complex mesh adaptation algorithms [13, 14]. On the other hand, the boundary elements method (BEM) deals only with integrals on the fluid boundaries [15–17] making remeshing, mesh refinement and interface position updating for drop deformation simpler to handle [18]. However, it is important to note that the classical BEM formulation in terms of only boundary integrals is valid only for Newtonian Stokes flows. The implementation of this type of BEM formulations when dealing with non-Newtonian fluids, i.e. variable viscosity, leads to boundary-domain integrals that require some particular schemes to deal with the domain part of the formulation, losing the advantage of boundary integrals alone.

In [1], the BEM is employed to model the deformation and motion of Newtonian drops suspended in a different moving Newtonian fluid. In this pioneer work, special attention was given to the evolution of the drops shape and possible break up conditions. More recently, several new BEM formulations have been developed to study two-dimensional drops deformation and motion, where the drops and/or the continuous phase are considered to be non-Newtonian fluids. However, these works usually consider rheological models independent of the local strain rate such as the Maxwell and Oldroyd-B models (for more details, see [9, 19]), which are insufficient for the analysis of shear thinning fluids. In these BEM formulations, various alternatives have been used to deal with the resulting domain integrals including transformations that eliminate the domain integrals [20], cell integration [19] and some forms of analytical approaches [21].

The deformation of a single shear thinning drop obeying the Carreau–Yasuda model (for details about this non-Newtonian model, see [22]) inside a convergent–divergent channel was evaluated by Khayat [18]. Even though the proposed formulation is based on a non-Newtonian model, the local effects are given in terms of an effective homogeneous viscosity inside the drop. The estimation of the effective viscosity is based on the rate of strain averaged over the region occupied by the drop at the prior time step. This characteristic of the solution scheme makes the formulation inadequate for long simulation spans and large drop deformations where the value of the local viscosity can greatly change from one point to another point inside the drop. It is important to point out that although the Carreau–Yasuda rheological model predicts accurately the dynamics of the flow motion of shear thinning fluids, it has the disadvantage of requiring the estimation of five parameters, which are often difficult to obtain. Some of the most widely accepted alternatives are the power and truncated power law models, see [12, 23]. The latter has the advantage of correctly representing both the power law and Newtonian behaviours of the viscosity, whereas the power law model shows shear thickening behaviour in shear thinning fluids in zones of low velocity gradients, see [23].

This study presents a BEM formulation for the simulation of the motion and deformation of non-Newtonian drops suspended in a Newtonian moving carrying fluid, where the fluid inside

DOI: 10.1002/fld

the drops behaves as a shear thinning fluid. An implicit velocity gradient calculation is used to obtain the corresponding non-Newtonian shear stresses, avoiding the problems that arise from space average schemes. In the integral representational formula for the interior flow, the dual reciprocity method (DRM), see [24, 25], is used to convert the domain integral resulting from the non-homogeneous (non-linear) term into equivalent boundary integrals, whereas the external Newtonian flow is directly represented in terms of boundary integrals according to the corresponding Green's integral representational formula. In this manner, an efficient boundary-only formulation of the problem is obtained. In order to represent adequately the actual physical behaviour of the system of drops, the truncated power law model is used to calculate implicitly the non-Newtonian viscosity at each collocation point. Various numerical schemes are employed in order to solve the obtained system of only boundary integral equations. Quadratic elements were used for the discretization of the surfaces and the approximation of the integral densities. It has been previously shown [26] that the use of this type of elements increases the accuracy of the approximation of the BEM–DRM formulation as well as being a mesh convergent discretization. The local values of the normal vector and curvature were calculated using fourth-order Lagrange polynomials, and a mass conservative surface smoothing algorithm was developed in order to provide the values of the polynomial coefficients with an adequate node distribution on the surface. Since during the simulation, the deformation of the drops can greatly increase their perimeters the drop surfaces are remeshed, if it is required, according to the magnitude of their deformation using the Bezier curves. Finally, the resulting non-linear system of algebraic equations obtained from the collocation on the surface and internal nodes was solved via a modified Newton–Raphson method, which showed good performance even on drops with strong non-Newtonian behaviour.

To test the performance of the developed formulation in a situation of physical significance without increasing the complexity of the analysis, a simple case of two initially circular shear thinning drops suspended in a Newtonian linear shear flow is considered. At the initiation of the numerical simulation, the two drops are located perpendicular to the streamlines of the imposed linear shear flow and the trajectories of their mass centres are followed during the simulations for a wide range of the physical and rheological parameters that describe the phenomena, namely the capillary number (Ca), viscosity ratio (λ) and power law index (n).

This paper is organized as follows. Governing equations for multiple non-Newtonian drops in an unbounded domain under Newtonian linear shear flow are presented in Section 2. In the same section, the selected rheological model is presented and its characteristics are briefly discussed. Table I gives a summary of the variables and parameters used in the mathematical formulation of the problem. Section 3 shows the integral representation of the problem as well as the DRM approximation used to convert the domain integral in the integral representational formula for the interior flow into equivalent boundary integrals. Section 3 also shows the calculation of the non-homogeneous (non-linear) term on the collocation points, as well as the function used to interpolate the different terms and to obtain the required particular solution of the auxiliary flow field. Section 4 presents the iterative scheme selected to solve the non-linear system of equations. Section 5 shows the different numerical algorithms that are used in conjunction with the boundary integral formulations to simulate the development of the drops as time progresses. In Section 6, results for drop interaction under different flow parameters are analysed and compared with those of Newtonian drops. Finally, conclusions regarding physical and numerical issues relating to the problem are given.

DOI: 10.1002/fld

Table I. Variables and parameters used.

S_p	surface of drop p
Ω_e	domain external to the drops
Ω_p	domain internal to drop p
u_j	fluid velocity, m/s
x_i	vector location of a given point, m
σ_{ij}	stress tensor, N/m^2
p	pressure, Pa
δ_{ij}	Kronecker delta
μ_e	external fluid viscosity, Pa s
τ_{ij}^{NN}	non-Newtonian viscous stress, N/m^2
$\eta(\dot{\gamma})$	non-Newtonian viscosity, Pa s
n_i	normal vector
$\dot{\gamma}$	second invariant of the deformation tensor, s^{-1}
ε_{ij}	deformation tensor, s^{-1}
G	shear rate of the base flow, s^{-1}
γ	surface tension, J/m^2
$\partial n_k/\partial x_k$	surface curvature, m^{-1}
k	power law consistency, Pa s
n	power law index
λ^{NN}	non-Newtonian viscosity ratio
Ca	capillary number
$u_i^j(x, y)$	single-layer kernel or Stokeslet
$K_{ij}(x, y)$	double-layer kernel or Stresslet
r	Euclidean distance between two points
τ_{ij}^e	extra stress tensor, N/m^2

2. GOVERNING EQUATIONS

The flow configuration under study is composed of m drops of a given non-Newtonian fluid, surrounded by a Newtonian fluid in an unbounded domain. A graphical representation of this set-up is shown in Figure 1 where S_p, $p=1,2,\ldots,m$, represents the boundary of each drop, Ω_e is the exterior flow domain and Ω_p, $p=1,2,\ldots,m$, the domain interior to each drop. Therefore, at each domain the flow field must satisfy the continuity and the momentum conservation equations that in the case of low Reynolds number reduces to the Stokes system of equations

$$\frac{\partial u_i}{\partial x_i}=0 \tag{1a}$$

$$\frac{\partial \sigma_{ij}}{\partial x_j}=0 \tag{1b}$$

DOI: 10.1002/fld

where

$$\sigma_{ij}=\begin{cases}-p\delta_{ij}+\mu_e\left(\dfrac{\partial u_i}{\partial x_j}+\dfrac{\partial u_j}{\partial x_i}\right), & x\in\Omega_e\\ -p\delta_{ij}+\tau_{ij}^{\mathrm{NN}}, & x\in\Omega_p,\quad p=1,2,\ldots,m\end{cases}\tag{2}$$

In Equations (1)–(2), $\mathbf{u}$ is the velocity, p the pressure, δ_{ij} the Kronecker delta, μ_e the viscosity of the external flow and τ_{ij}^{NN} is the non-Newtonian stress tensor given by

$$\tau_{ij}^{\mathrm{NN}}=\eta(\dot{\gamma})\left(\frac{\partial u_i}{\partial x_j}+\frac{\partial u_j}{\partial x_i}\right)\tag{3}$$

where $\eta(\dot{\gamma})$ is the non-Newtonian viscosity and

$$\dot{\gamma}=\sqrt{2\sum_{i=1}^{2}\sum_{j=1}^{2}\varepsilon_{ij}\varepsilon_{ij}}\tag{4}$$

with

$$\varepsilon_{ij}=\frac{1}{2}\left(\frac{\partial u_i}{\partial x_j}+\frac{\partial u_j}{\partial x_i}\right)\tag{5}$$

The external flow field must also satisfy the following asymptotic conditions:

$$\mathbf{u}\to\mathbf{u}^{\infty},\quad p\to p^{\infty}\quad \text{as } |x|\to\infty\tag{6}$$

where $\mathbf{u}^{\infty}$ and p^{∞} are, respectively, the velocity and pressure far away from the drops. In this study, the asymptotic condition is a simple shear flow given by

$$\mathbf{u}^{\infty}(x)=(Gx_2,0)\tag{7}$$

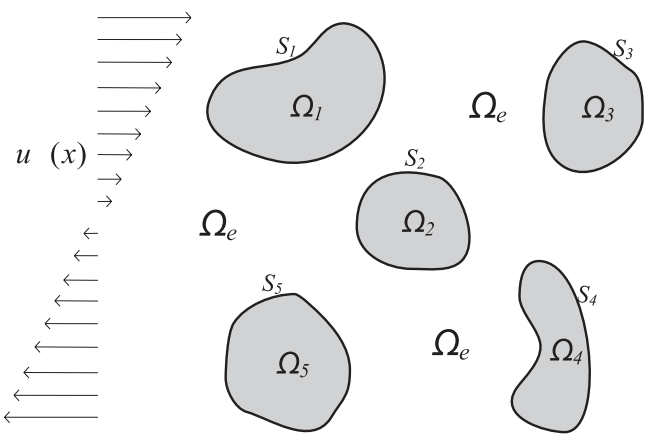

Figure 1. Typical schematic representation of particles in Stokes shears flow.

DOI: 10.1002/fld

with a corresponding constant pressure, where G is the shear rate of the flow. Velocity and surface traction matching conditions on the drops surface are

$$[\mathbf{u}]_{S_p}=0 \quad \text{and} \quad [\sigma_{ij}\ \ n_j]_{S_p}=\gamma n_i \frac{\partial n_k}{\partial x_k},\ \ p=1,2,\ldots,m \tag{8}$$

where $[\ ]_{S_p}$ denotes the jump across the drop surface S_p from Ω_e to Ω_p. In (8), γ is the surface tension, $\mathbf{n}$ is the outward unit normal vector and $\partial n_k/\partial x_k$ is the surface curvature.

Besides, at the drop surface the following kinematic condition needs to be satisfied:

$$\frac{\mathrm{d}\mathbf{x}(\xi)}{\mathrm{d}t}=\mathbf{u}(\xi) \tag{9}$$

with $\mathbf{u}(\xi)$ is the drop surface velocity.

As the imposed external flow field is a regular Stokes flow, it follows from the domain integration of the momentum (1b) over the unbounded external domain that the net force exerted over all the particles needs to be equal to zero, i.e.

$$\int_S \sigma_{ij} n_j \,\mathrm{d}S=0 \tag{10}$$

where S is the union of all of the drop surfaces considered, i.e. $S=\bigcup_{p=1}^{m} S_p$.

2.1. Non-Newtonian stress tensor

An adequate rheological model must be selected in order to accurately simulate a given physical system. In the case of shear thinning drops, the power law model has been shown to be a powerful tool bringing together accuracy and simplicity. Unfortunately, this model predicts shear thickening in shear thinning drops in zones where velocity gradients are low, see [22, 23]. The truncated power law model corrects the standard power law deficiencies for low deformation tensor by including an additional parameter $\dot{\gamma}_0$ that defines a transition from a Newtonian to a power law behaviour in the viscosity

$$\eta(\dot{\gamma})=\begin{cases} k\left(\dfrac{\dot{\gamma}}{\dot{\gamma}_0}\right)^{n-1}, & \dot{\gamma}\geqslant\dot{\gamma}_0 \\ k, & \dot{\gamma}<\dot{\gamma}_0 \end{cases} \tag{11}$$

where k is the power law consistency and n the power law index, which determines the strength of the non-Newtonian effect. For shear thinning fluids values of the power law index vary in the range $[0.2, 0.8]$ (see [22]). Using this model, shear thinning fluids will behave as a Newtonian fluid up to $\dot{\gamma}=\dot{\gamma}_0$, in accordance with the experimentally observed behaviour of this type of fluids, see [11].

Equations (2) and (3) can be expressed in the non-dimensional form as

$$\sigma_{ij}=-p\delta_{ij}+\left(\frac{\partial u_i}{\partial x_j}+\frac{\partial u_j}{\partial x_i}\right) \tag{12}$$

DOI: 10.1002/fld

for $x \in \Omega_e$ and

$$\sigma_{ij} = \begin{cases} -p\delta_{ij} + \lambda^{\mathrm{NN}} \left(\dfrac{\dot{\gamma}}{\dot{\gamma}_0} \right)^{n-1} \left(\dfrac{\partial u_i}{\partial x_j} + \dfrac{\partial u_j}{\partial x_i} \right), & \dot{\gamma} \geqslant \dot{\gamma}_0 \\ -p\delta_{ij} + \lambda^{\mathrm{NN}} \left(\dfrac{\partial u_i}{\partial x_j} + \dfrac{\partial u_j}{\partial x_i} \right), & \dot{\gamma} < \dot{\gamma}_0 \end{cases} \tag{13}$$

for $x \in \Omega_p$, $p = 1, 2, \ldots, m$, where the reference length is set as the radius of the non-deformed drop a, reference velocity γ/μ_e, reference pressure γ/a, reference time $\mu_e a/\gamma$ and the non-Newtonian viscosity ratio as $\lambda^{\mathrm{NN}} = k/\mu_e$.

In order to represent the interior flow field, in the case when $\dot{\gamma} > \dot{\gamma}_0$ as a non-homogeneous Stokes flow field, the internal traction (13) is rewritten as

$$\sigma_{ij} = \sigma_{ij}^{\mathrm{N}} + \lambda^{\mathrm{NN}} \left(\frac{\dot{\gamma}}{\dot{\gamma}_0} \right)^{n-1} \left(\frac{\partial u_i}{\partial x_j} + \frac{\partial u_j}{\partial x_i} \right) - \lambda^{\mathrm{N}} \left(\frac{\partial u_i}{\partial x_j} + \frac{\partial u_j}{\partial x_i} \right) = \sigma_{ij}^{\mathrm{N}} + \tau_{ij}^{e} \tag{14}$$

where

$$\sigma_{ij}^{\mathrm{N}} = -p\delta_{ij} + \lambda^{\mathrm{N}} \left(\frac{\partial u_i}{\partial x_j} + \frac{\partial u_j}{\partial x_i} \right) \tag{15}$$

and λ^{N} is an artificial fluid viscosity chosen in this study to be equal to λ^{NN}, such that a power index $n = 1$ corresponds to a Newtonian fluid.

The term τ_{ij}^{e} is the extra stress tensor, and it accounts for the non-Newtonian effects in the viscosity, i.e.

$$\tau_{ij}^{e} = \left(\lambda^{\mathrm{NN}} \left(\frac{\dot{\gamma}}{\dot{\gamma}_0} \right)^{n-1} - \lambda^{\mathrm{N}} \right) \left(\frac{\partial u_i}{\partial x_j} + \frac{\partial u_j}{\partial x_i} \right) \tag{16}$$

With the new definition of traction (14), the momentum equation (1b) for any point $x \in \Omega_p$ is given by

$$\frac{\partial \sigma_{ij}}{\partial x_j} = \frac{\partial \sigma_{ij}^{\mathrm{N}}}{\partial x_j} + \frac{\partial \tau_{ij}^{e}}{\partial x_j} = 0 \tag{17}$$

In terms of the dimensional variables, the matching, asymptotic and kinematic conditions become

$$[\mathbf{u}]_{S^p} = 0 \tag{18a}$$

$$[\sigma_{ij} \;\; n_j]_{S^p} = n_i \frac{\partial n_k}{\partial x_k} \tag{18b}$$

$$\mathbf{u}^{\infty}(x) = (Ca\, x_2, 0), \quad p^{\infty}(x) = \mathrm{const} \tag{19}$$

$$\frac{\mathrm{d}\mathbf{x}(\xi)}{\mathrm{d}t} = \mathbf{u}(\xi) \tag{20}$$

where Ca is the capillary number given by $Ca = Ga\mu_e/\gamma$. In this manner, the three dimensionless parameters defining the behaviour of the drops motion and deformation are Ca, λ^{NN} and n.

DOI: 10.1002/fld

3. INTEGRAL REPRESENTATION

Using the Green's formulae for a homogeneous Stokes system of equations, as is the case of Equations (1a) and (1b) for the exterior Newtonian flow, the following integral representation for the velocity field outside the drops can be obtained:

$$C_{ij}u_j(x)+\int_S K_{ij}(x,y)(u_j(y))_e\,\mathrm{d}S_y = u_i^{\infty}(x)+\int_S u_{ij}(x,y)(\sigma_{jk}(\mathbf{u}(y)))_e n_k(y)\,\mathrm{d}S_y \tag{21}$$

where $(u_j(y))_e$ and $(\sigma_{jk}(\mathbf{u}(y)))_e$ are the values of the surface velocity and stress, respectively, at a point $y\in S$ coming from Ω_e. In the above integral representational formula, $u_i^j(x,y)$ is the single-layer kernel or Stokeslet, located at point y and oriented in the jth direction, $K_{ji}(y,\xi)$ is the double-layer kernel or Stresslet and C_{ij} is a constant coefficient equal to $C_{ij}=\delta_{ij}$ when $x\in\Omega_e$, $C_{ij}=1/2\delta_{ij}$ when $x\to\xi\in S$ and $C_{ij}=0$ when $x\notin\Omega_e$.

The expressions for $u_{ij}(x,y)$ and $K_{ji}(y,\xi)$ in a two-dimensional field are given by

$$u_{ij}(x,y)=-\frac{1}{4\pi}\left[\ln\left(\frac{1}{r}\right)\delta_{ij}+\frac{(x_i-y_i)(x_j-y_j)}{r^2}\right] \tag{22}$$

$$K_{ij}(x,y)=\sigma_{ij}(u_i^j)n_k(y)=-\frac{1}{\pi}\frac{(x_i-y_i)(x_j-y_j)(x_k-y_k)n_k(y)}{r^4} \tag{23}$$

where $r=|x-y|$ is the Euclidean distance between points x and y.

As the net force exerted by the exterior flow over all the drops is zero (see Equation (10)), which implies zero average density of the single-layer potential in Equation (21), it follows that such a single-layer integral tends to zero at infinity as $O(1/r)$. This behaviour of the single layer guarantees that the velocity field defined by Equation (21) satisfies the asymptotic condition (6).

On the other hand, the velocity field inside a drop p, with surface boundary S_p and internal domain Ω_p, can be expressed by the Green's integral representational formula for the non-homogeneous Stokes flow field (17) as

$$C_{ij}u_j(x)-\int_{S_p}K_{ij}(x,y)(u_j(y))_p\,\mathrm{d}S_y=\frac{1}{\lambda^{\mathrm{N}}}\int_{\Omega p}u_{ij}(x,y)\left(-\frac{\partial\tau_{jk}^e}{\partial x_k}\right)\mathrm{d}\Omega_y - \frac{1}{\lambda^{\mathrm{N}}}\int_{S_p}u_{ij}(x,y)(\sigma_{jk}^{\mathrm{N}}(\mathbf{u}(y)))_p n_k(y)\,\mathrm{d}S_y \tag{24}$$

As before, the constant C_{ij} is equal to $C_{ij}=\delta_{ij}$ when $x\in\Omega_p$, $C_{ij}=1/2\delta_{ij}$ when $x\to\xi\in S_p$ and $C_{ij}=0$ when $x\notin\Omega_p$. In this case, $(u_j(y))_p$ and $(\sigma_{jk}(\mathbf{u}(y)))_p$ are the values of the surface velocity and stress at a point $y\in S_p$ coming from Ω_p. Using a similar approach, it is possible to show that the following integral relation holds for any other drop $r\neq p$, at a collocation point $x\in\overline{\Omega}_p$.

$$-\int_{S_r}K_{ij}(x,y)(u_j(y))_r\,\mathrm{d}S_y=\frac{1}{\lambda^{\mathrm{N}}}\int_{\Omega_r}u_{ij}(x,y)\left(-\frac{\partial\tau_{jk}^e}{\partial x_k}\right)\mathrm{d}\Omega_y - \frac{1}{\lambda^{\mathrm{N}}}\int_{S_r}u_{ij}(x,y)(\sigma_{jk}^{\mathrm{N}}(\mathbf{u}(y)))_r n_k(y)\,\mathrm{d}S_y \tag{25}$$

DOI: 10.1002/fld

By adding to Equation (24) the sum of the integral relation (25) corresponding to all the other drops, i.e. $\sum_{r=1(r\neq p)}^{m}$, we obtain the following representational formula for the velocity field at a point $x\in\overline{\Omega}_p$, i.e. at a drop p, in terms of surface and domain integrals over all the drops:

$$C_{ij}u_j(x)-\int_S K_{ij}(x,y)(u_j(y))_i\,\mathrm{d}S_y=\frac{1}{\lambda^{\mathrm{N}}}\int_{\Omega_i}u_{ij}(x,y)\left(-\frac{\partial\tau^e_{jk}}{\partial x_k}\right)\mathrm{d}\Omega_y$$
$$-\frac{1}{\lambda^{\mathrm{N}}}\int_S u_{ij}(x,y)(\sigma^{\mathrm{N}}_{jk}(\mathbf{u}(y)))_i n_k(y)\,\mathrm{d}S_y \tag{26}$$

where $\Omega_i=\bigcup_{j=1}^{m}\Omega_j$ is the domain interior to all the particles, and $(u_j(y))_i$ and $(\sigma_{jk}(\mathbf{u}(y)))_i$ are the values of the surface velocity and stress at a point $y\in S$ coming from Ω_i.

By evaluating Equations (21) and (26) at a point $x\to\xi\in S_p$, i.e. at the surface of a drop p, and using the velocity matching condition across the drop surface, Equation (18a), the following system of integral equation is obtained:

$$\frac{(1+\lambda^{\mathrm{N}})}{2}u_i(\xi)+(1-\lambda^{\mathrm{N}})\int_S K_{ij}(\xi,y)u_j(y)\,\mathrm{d}S_y$$
$$=u_i^{\infty}(\xi)+\int_{\Omega_i}u_{ij}(\xi,y)\left(-\frac{\partial\tau^e_{jk}}{\partial x_k}\right)\mathrm{d}\Omega_y$$
$$+\int_S u_{ij}(\xi,y)[(\sigma_{jk}(\mathbf{u}(y))n_k(y))_e-(\sigma^{\mathrm{N}}_{jk}(\mathbf{u}(y))n_k(y))_i]\,\mathrm{d}S_y \tag{27}$$

where according to (18a) $(u_j(y))_e=(u_j(y))_i=u_j(y)$.

Since the internal traction in (27) is the Newtonian traction σ^{N}_{ij}, the boundary conditions for the traction jump (18b) cannot be directly applied. Using Equation (14), the boundary condition for the traction jump becomes

$$(\sigma_{jk}(\mathbf{u}(y))n_k(y))_e-(\sigma^{\mathrm{N}}_{jk}(\mathbf{u}(y))n_k(y))_i=(\tau^e_{ik}n_k)_i+n_i\frac{\partial n_k}{\partial x_k} \tag{28}$$

Substituting (28) into (27) the following non-linear system of integral equations for the surface velocity, at a point $x\to\xi\in S_p$, is obtained:

$$u_i(\xi)+\frac{2(1-\lambda^{\mathrm{N}})}{(1+\lambda^{\mathrm{N}})}\int_S K_{ij}(\xi,y)u_j(y)\,\mathrm{d}S_y=F_i^{\mathrm{NN}}(\xi) \tag{29}$$

with

$$F_i^{\mathrm{NN}}(\xi)=\frac{2}{(1+\lambda^{\mathrm{N}})}\left[u_i^{\infty}(\xi)+\int_{\Omega_i}u_{ij}(\xi,y)\left(-\frac{\partial\tau^e_{jk}}{\partial x_k}\right)\mathrm{d}\Omega_y\right.$$
$$\left.+\int_S u_{ij}(\xi,y)(\tau^e_{jk}n_k(y))_i\,\mathrm{d}S_y+\int_S u_{ij}(\xi,y)n_i\frac{\partial n_k}{\partial x_k}\,\mathrm{d}S_y\right] \tag{30}$$

DOI: 10.1002/fld

In [2] it is proven that the homogeneous form of Equation (29) does not have any poles in the range $0<\lambda^{\mathrm{N}}<\infty$ and consequently (29) has a unique solution for any continuous datum $F_i(\xi)$ in this range of λ^{N}. Therefore, at each step of an iterative solution of (29), it is guaranteed that the integral equation has a unique solution, where at each iteration the value of τ^e_{jk} is considered to be known.

3.1. Treatment of domain integrals

To transform the domain integral in (30) into an equivalent series of surface integrals, the DRM is employed. The basis of this method is the expansion of the non-homogeneous term in the governing equations using the interpolation approximation

$$-\frac{\partial \tau^e_{jk}}{\partial x_k} \approx \sum_{k=1}^{n} f(x, z^k)\alpha_l^k \delta_{jl} \tag{31}$$

where $f(x, z^k)$ is a known set of interpolating functions (usually radial basis functions) and α_l^k is an unknown vector of coefficients to be determined by collocation at the points z^k $(k=1, 2, 3, \ldots, n)$ in the domain of interest where the non-homogeneous term is to be approximated. Using this approximation, we found the following expression for the volume integral over the bounded domain Ω_p at a drop p (for more details, see [24]):

$$\int_{\Omega_p} u_{ij}(x, y)\left(-\frac{\partial \tau^e_{jk}}{\partial x_k}\right) \mathrm{d}\Omega_y = \sum_{k=1}^{n(p)} \alpha_l^{p,k} \int_{\Omega_p} u_{ij}(x, y) f(y, z^{p,k})\delta_{jl}\, \mathrm{d}\Omega_y \tag{32}$$

for every $x \in R^2$ and $n(p)$ interpolation points $z^{p,k} \in \overline{\Omega}_p$, with $k=1, 2, 3, \ldots, n(p)$, usually distributed on the surface and at the interior of the interpolating domain.

Applying the Green's second identity to the flow field $(u_{ij}(x, y)e_i, p_j(x, y))$ and the auxiliary field $(\hat{u}_{il}(y, z^{p,k})e_i, \hat{p}_l(y, z^{p,k}))$ in the bounded domain Ω_p, where

$$\frac{\partial^2 \hat{u}_{il}(y, z^{p,k})}{\partial y_j \partial y_j} - \frac{\partial \widehat{p}_l(y, z^{p,k})}{\partial y_i} = f(y, z^{p,k})\delta_{il} \tag{33}$$

$$\frac{\partial \hat{u}_{il}(y, z^{p,k})}{\partial y_i} = 0 \tag{34}$$

the following expression for the domain integrals at the right-hand side of (32) in terms of surface integrals only is obtained:

$$\begin{aligned}\int_{\Omega_p} u_{ij}(x, y) f(y, z^{p,k})\delta_{jl}\, \mathrm{d}\Omega_y \; &= C_{ij}\hat{u}_{jl}(x, z^{p,k}) - \int_{S_p} K_{ij}(x, y)\hat{u}_{jl}(y, z^{p,k})\, \mathrm{d}S_y \\ &\quad + \int_{S_p} u_{ij}(x, y)\hat{t}_{jl}(y, z^{p,k})\, \mathrm{d}S_y \end{aligned} \tag{35}$$

where

$$\hat{t}_{il}(y, z^{p,k}) = \sigma_{ij}(\hat{u}_{il}(y, z^{p,k})e_i, \widehat{p}_l(y, z^{p,k}))n_j(y) \tag{36}$$

DOI: 10.1002/fld

In this manner, the volume integral in (24), for a point $x \in \overline{\Omega}_p$, can be approximated by

$$\int_{\Omega_p} u_{ij}(x,y)\left(-\frac{\partial \tau^e_{jk}}{\partial x_k}\right) \mathrm{d}\Omega_y = \sum_{k=1}^{n(p)} \alpha_l^{p,k} \left[C_{ij}\hat{u}_{jl}(x,z^{p,k}) - \int_{S_p} K_{ij}(x,y)\hat{u}_{jl}(y,z^{p,k})\,\mathrm{d}S_y + \int_{S_p} u_{ij}(x,y)\hat{t}_{jl}(y,z^{p,k})\,\mathrm{d}S_y \right] \tag{37}$$

with C_{ij} equal to $C_{ij}=\delta_{ij}$ when $x \in \Omega_p$ and $C_{ij}=1/2\delta_{ij}$ when $x \to \xi \in S_p$.

In the same manner, it is possible to show that the volume integral over the bounded domain Ω_r in (25), for a point $x \in \overline{\Omega}_p$, can be given in terms of its DRM approximation as

$$\int_{\Omega_r} u_{ij}(x,y)\left(-\frac{\partial \tau^e_{jk}}{\partial x_k}\right) \mathrm{d}\Omega_y = \sum_{k=1}^{n(r)} \alpha_l^{r,k} \left[-\int_{S_r} K_{ij}(x,y)\hat{u}_{jl}(y,z^{r,k})\,\mathrm{d}S_y + \int_{S_r} u_{ij}(x,y)\hat{t}_{jl}(y,z^{r,k})\,\mathrm{d}S_y \right] \tag{38}$$

with $n(r)$ interpolation points $z^{r,k} \in \overline{\Omega}_r$, $k=1,2,3,\ldots,n(r)$.

Substituting the above volume integrals in Equations (24) and (30), we obtain the following system of boundary-only integral equations:

$$\begin{aligned} & C_{ij}u_j(x) - \int_{S_p} K_{ij}(x,y)(u_j(y))_i\,\mathrm{d}S_y \\ &= -\frac{1}{\lambda^{\mathrm{N}}}\int_{S_p} u_{ij}(x,y)(\sigma^{\mathrm{N}}_{jk}(\mathbf{u}(y)))_i n_k(y)\,\mathrm{d}S_y + \frac{1}{\lambda^{\mathrm{N}}}\sum_{k=1}^{n(p)} \alpha_l^{p,k}\left[C_{ij}\hat{u}_{jl}(x,z^{p,k}) \right. \\ &\quad \left. - \int_{S_p} K_{ij}(x,y)\hat{u}_{jl}(y,z^{p,k})\,\mathrm{d}S_y + \int_{S_p} u_{ij}(x,y)\hat{t}_{jl}(y,z^{p,k})\,\mathrm{d}S_y \right] \end{aligned} \tag{39}$$

for a point $x \in \overline{\Omega}_p$, with C_{ij} equal to $C_{ij}=\delta_{ij}$ when $x \in \Omega_p$ and $C_{ij}=1/2\delta_{ij}$ when $x \to \xi \in S_p$, and

$$\begin{aligned} & u_i(\xi) + \frac{2(1-\lambda^{\mathrm{N}})}{(1+\lambda^{\mathrm{N}})}\int_S K_{ij}(\xi,y)u_j(y)\,\mathrm{d}S_y \\ &= \frac{2}{(1+\lambda^{\mathrm{N}})}\left\{ u_i^{\infty}(\xi) + \int_S u_i^j(\xi,y) n_i \frac{\partial n_k}{\partial x_k}\,\mathrm{d}S_y + \int_S u_i^j(\xi,y)(\tau^e_{jk}n_k(y))_i\,\mathrm{d}S_y \right. \\ &\quad + \sum_{k=1}^{n(p)} \alpha_l^{p,k}\left[\frac{1}{2}\hat{u}_i(\xi,z^{p,k}) - \int_{S_p} K_{ij}(\xi,y)\hat{u}_{jl}(y,z^{p,k})\,\mathrm{d}S_y + \int_{S_p} u_{ij}(\xi,y)\hat{t}_{jl}(y,z^{p,k})\,\mathrm{d}S_y \right] \\ &\quad \left. + \sum_{r=1(r\neq p)}^{m}\sum_{k=1}^{n(r)} \alpha_l^{r,k}\left[-\int_{S_r} K_{ij}(x,y)\hat{u}_{jl}(y,z^{r,k})\,\mathrm{d}S_y + \int_{S_r} u_{ij}(x,y)\hat{t}_{jl}(y,z^{r,k})\,\mathrm{d}S_y \right] \right\} \end{aligned} \tag{40}$$

DOI: 10.1002/fld

for a point $\xi \in S_p$. In the above expressions the subscripts refer to vectors and tensor indexes and the superscripts refer to summation indexes.

The values of the coefficients $\alpha_l^{r,k}, r=1,2,\ldots,m,$ in the above system of integral equations, corresponding to the interpolation at the domains interior to each drop, can be calculated from (31) in the following manner, using matrix notation:

$$\{\alpha_l^r\} = [F]^{-1} \left\{ -\frac{\partial \tau_{jk}^e(x)}{\partial x_k} \delta_{jl} \right\}_r \tag{41}$$

At this point of the formulation, a numerical procedure must be established in order to relate the nodal values of the velocity field to the divergence of the non-Newtonian stress tensor at the collocation points. A common procedure to obtain such an expression when using the DRM is to express the velocity field at an interpolation point in terms of the function $f(x, y^k)$ as

$$u_i^{(t)} \approx \sum_{k=1}^{n} f(x, y^k)(\beta_i^k)^{(t)} \tag{42}$$

which can be expressed in matrix notation as

$$\{u_i^{(t)}\} = [F]\{\beta_i^{(t)}\} \quad \text{with } \{\beta_i^{(t)}\} = [F]^{-1}\{u_i^{(t)}\} \tag{43}$$

where the superscript (t) is representative of the iteration step in the approximation of the non-linear term (see Section 4). Using (43), the gradient of the velocity field at the interpolation points can be given in terms of the values of the velocity field at those points by

$$\left\{ \frac{\partial u_i^{(t)}}{\partial x_j} \right\} = \left[\frac{\partial F}{\partial x_j} \right] \{\beta_i^{(t)}\} = \left[\frac{\partial F}{\partial x_j} \right] [F]^{-1} \{u_i^{(t)}\} \tag{44}$$

This approximation is used at each drop to express the extra stress tensor τ_{ij}^e in terms of the drop surface and internal velocities. A similar approach was used to obtain an expression of the divergence of τ_{ij}^e in terms of its nodal values. In this manner, the coefficients $\boldsymbol{\alpha}^r, r=1,2,\ldots,m,$ in the integral equation (40) are defined in terms of the corresponding drops surface and internal velocities. Therefore, integral equation (40) defines a relation between the surface velocity at a drop p in terms of the surface and interior velocities of all the drops. By evaluating Equation (39) at the surface and internal points of each drop, two additional sets of integral equations for each drop is obtained, which are used to complete the system of equations, together with (40). In Equation (39), the coefficients $\boldsymbol{\alpha}^p$ are given in terms of the surface and internal drop velocities using relation (44). From the solution of (40) at the surface of each drop and (39) at the surface and interior points of each drop the values of the drops surface and internal velocities as well as the surface Newtonian traction $\sigma_{jk}^{\mathrm{N}}(\mathbf{u})n_k$ are obtained.

In this study, we use the augmented thin plate spline $f(x, y^k) = r^2(x, y^k)\log(r(x, y^k)) + P_1(x)$ as the interpolating function, where $P_1(x)$ is a polynomial of order 1. This function has shown to be an accurate and simple alternative for use within the DRM approach (see [27–29]). For the above interpolation function the analytical expression of the auxiliar field $(\hat{u}_{il}(y, z^{p,k})e_i, \hat{p}_l(y, z^{p,k}))$ is known and available in the open literature (see [27, 30]).

DOI: 10.1002/fld

4. ITERATIVE SOLUTION OF THE NON-LINEAR SYSTEM OF EQUATIONS FOR EACH TIME STEP

After discretization of the system of integral equations, a non-linear system of algebraic equations arises for the variables u_i at points $\xi \in S$ and $x \in \Omega_p$, and σ_{ij}^{N} at $\xi \in S$. Given the non-linear character of this system caused by the dependence of τ_{ij}^{e} on the nodal velocities, an iterative procedure must be set in place to determine the actual solution. For simplicity, the system of algebraic equations obtained after the discretization and interpolation can be expressed in matrix form as

$$[A][\mathbf{X}] = [\mathbf{C}] + [\mathbf{B}(\mathbf{X})] \tag{45}$$

where the matrix A contains the coefficients of the variables X to be found (velocities at the drops surface and interior domains as well as the Newtonian surface tractions), the vector C contains the non-homogeneous terms and B the results of using the previous iteration to calculate the terms related to the DRM approximation.

The solution of this complete system of equations can be sought in different ways, the most common of which is the Picard iteration because it reduces the solution of the non-linear system of equations to the successive solution of a similar non-homogeneous linear system. Even though this is by far the simplest and computational less expensive method, it was found to diverge when the power law index was smaller than ≈ 0.8, and therefore not used here. A good alternative is to use the Newton–Raphson method. The method starts by defining the residual function $W(\mathbf{X})$,

$$W(\mathbf{X}) = A\mathbf{X} - \mathbf{B}(\mathbf{X}) - C \tag{46}$$

The objective is then to find a vector $\mathbf{X}$ that minimizes $W(\mathbf{X})$. In order to do so, a Taylor series expansion of $W(\mathbf{X})$ around an N-dimensional point $\mathbf{X}^{(t)}$ truncated on the linear term is used, i.e.

$$W(\mathbf{X}) \approx W(\mathbf{X}^{(t)}) + \frac{1}{\phi^{(t)}} J_X(\mathbf{X}^{(t)}) \cdot \Delta\mathbf{X}^{(t)} = 0 \tag{47}$$

where J_X is the Jacobian matrix and

$$\Delta\mathbf{X}^{(t)} = (\mathbf{X}^{(t+1)} - \mathbf{X}^{(t)}) \tag{48}$$

Equation (47) constitutes a linear system of equations. Once the values of $\Delta\mathbf{X}^{(t)}$ are known, the value of $\mathbf{X}^{(t+1)}$ is calculated and the process is repeated until convergence is achieved.

The standard Newton–Raphson method uses the value of $\phi^{(t)} = 1$ in (47), but in most cases this approach will overshot the right answer and even diverge. In order to avoid such situations, the value of $\phi^{(t)}$ can be calculated as, see [31]

$$\phi_{\mathrm{optimal}}^{(t)} \approx \left(\frac{\|W(\mathbf{X}^{(t+1)})\|^2}{\|W(\mathbf{X}^{(t)})\|^2} + 1 \right)^{-1} \tag{49}$$

It has been shown that close to the solution of a non-linear system the use of $\phi_{\mathrm{optimal}}^{(t)}$ can lead to a situation where the convergence is lost. A common approach is to initially employ the full step size $\phi^{(t)} = 1$, and only after checking that the problem is diverging, calculate and use $\phi_{\mathrm{optimal}}^{(t)}$.

DOI: 10.1002/fld

In order to check for convergence of the iterative approach, two convergence criteria are used. The first option is to calculate the error $e^{(t)}$ as the norm of the residual

$$e_1^{(t)} = \|W(\mathbf{X}^{(t)})\| = \|A\mathbf{X}^{(t)} - \mathbf{B}(\mathbf{X}^{(t)}) - C\| \tag{50}$$

Convergence of the iterative scheme was assumed when $e_1^{(t)} \leqslant p \times 10^{-8}$ where p is the total number of collocation points both on the surface and inside the drop. The second option is related to the change in the velocity field at each collocation point at every iteration

$$e_2^{(t)} = \max_{m=1,p} \left[\frac{|u_i^{(t)}(y^m) - u_i^{(t-1)}(y^m)|}{|u_i^{(t-1)}(y^m)|}, \ \forall u_i^{(t-1)}(y^m) \neq 0 \right] \tag{51}$$

and $i = 1, 2$.

The main drawback of this approach is that it can find convergence on a local minimum, even if the objective function $W(\mathbf{X})$ is still far from 0. This is even more evident when the calculated value of $\phi_{\text{optimal}}^{(t)}$ for a given iteration is very small. In view of this behaviour, the convergence criteria of $e_2^{(t)}$ is only used if $e_2^{(t)} \leqslant 10^{-4}$ and $e_1^{(t)} \leqslant p \times 10^{-6}$.

5. NUMERICAL IMPLEMENTATION

In the numerical solution of the obtained boundary-only system of integral equations, the surface of the drops as well as the unknown surface densities are approximated using quadratic isoparametric boundary elements. The resulting set of integrals are regular and can be evaluated using standard Gaussian quadratures. There is a small numerical difficulty in calculating the integral kernels when integration is made over the same element where the source point is located. In such cases it is recommended to use an integral transformation such as Telles' Transformation to evaluate the single layer weak singular integral and Rigid Body analogy in the case of the double layer kernel. Details on these procedures can be found in [17, 32].

Since the traction discontinuity across the drop surface is a function of the local values of the normal vector and curvature, it is necessary to have a good estimation of these two surface quantities in order to simulate accurately the corresponding drops deformation. In the evaluation of these two surface quantities, the first issue to consider is the type of interpolation used in the local representation of the drop boundary. There are different alternatives to interpolate the drop surface, including high-order schemes such as the Bezier curves, Legender polynomials and radial basis functions. In this study, the normal vector and curvature are obtained from a local interpolation of the surface points in terms of a Lagrange polynomial. The choice of this type of interpolation is due to their ability to approximate complicated nodal distributions in a simple way and in particular the simplicity in the evaluation of their first and second directional derivatives required to obtaining the values of the surface normal vector and curvature [3].

Having selected Lagrange polynomials as the interpolation functions, the second issue to consider is their degree. Low-order polynomials have the advantage of simplicity in their formulation and stability of the obtained drop evolution due to the smoothness of the surface interpolation. Unfortunately, the use of this type of polynomials can show great variations on the calculated value of the normal vector and curvature over small distances, due to their dependence on only few

DOI: 10.1002/fld

neighboring nodes. On the other hand, the use of higher-order polynomials, which requires a larger number of nodes in the local interpolation, usually results in a gradual variation on the estimated values of the normal vector and curvature. However, their use can induce large oscillations between the interpolation points when the nodal positions are not evenly distributed. This type of oscillations often affects the stability of the obtained drop evolution. Taking all of this into consideration, this work uses a fourth-order polynomial to locally approximate the drop surface for the calculation of the normal vector and curvature. The point where these values are calculated is the central point of the polynomial (node 3) and two more nodes are considered at each side. The normal vector is obtained by the expression

$$\mathbf{n} = \frac{1}{\sqrt{(x_1')^2 + (x_2')^2}} \begin{pmatrix} x_2' \\ -x_1' \end{pmatrix} \tag{52}$$

and the curvature calculated by

$$\frac{\partial n_k}{\partial x_k} = \frac{x_1' x_2'' - x_2' x_1''}{((x_1')^2 + (x_2')^2)^{3/2}} \tag{53}$$

where

$$x_i' = \tfrac{1}{6}(x_i^{(1)} - 8x_i^{(2)} + 8x_i^{(4)} - x_i^{(5)}) \tag{54}$$

$$x_i'' = \tfrac{1}{3}(-x_i^{(1)} + 16x_i^{(2)} - 30x_i^{(3)} + 16x_i^{(4)} - x_i^{(5)}) \tag{55}$$

To reduce the effect of undesired interpolation oscillations a remeshing algorithm is implemented that redistribute uniformly the surface points (for more details, see Section 5.1). The approximations employed to calculate the normal vector and curvature are valid for any type of two-dimensional drop surfaces. However, in cases where there is a strong deformation on the drop surface or close to a drop break up it is necessary to include a remeshing algorithm that could increase the nodal density near such surface irregularities or instead it is also possible to change the type of interpolation in those regions. This type of adjusted interpolation in regions of strong deformations in the case of three-dimensional Newtonian drops was implemented by Cristini *et al.* [33].

Trajectories and deformation of the drops are computed by advancing the surface nodes according to the kinematical condition, Equation (9), integrated using a second-order Runge–Kutta scheme [5] with time steps $\Delta t = 0.01\, Ca^{-1}$. Results were unaffected by smaller time steps but were unstable for larger steps when large deformations were taken into consideration.

5.1. Mass conservative surface smoothing

The mathematical characteristics of numerical differentiation on the evaluation of the normal vector and the curvature make those expressions rather sensitive to oscillations in the nodal positions at the drop surface. This problem becomes even greater in time-advancing schemes because initially small oscillations tend to grow creating rough surfaces where polynomials are no longer capable of approximating the surface correctly. Taking this into account, a numerical scheme must be implemented to smooth the surface after a given number of time steps.

In this work, a mass conservative scheme was developed to avoid the mass loss while maintaining good smoothing behaviour and low computational cost. The first step is to consider a section S_C of the surface composed by two adjacent quadratic elements, i.e. consisting of five surface nodes,

DOI: 10.1002/fld

in which the common node between the elements is the one to be smoothed and the remaining two nodes are those located on either side. The area of the strip between this section of the boundary curve and the horizontal axes (x_1 axes) is given by

$$A_{S_C} = \int_{S_C} x_2 \, \mathrm{d}x_1 = \int_{S_{C,\text{left}}} x_2 \, \mathrm{d}x_1 + \int_{S_{C,\text{right}}} x_2 \, \mathrm{d}x_1 \tag{56}$$

Each of the integrals in expression (56) is evaluated by standard Gaussian quadratures using quadratic interpolation functions. Then a new fourth degree element is chosen to represent the same surface section. The new interpolation functions require five nodes that in this case are the same five nodes that originally composed the two quadratic elements in (56). Applying Gaussian quadratures to evaluate A_{S_C} at the new fourth-order element, the following expression is obtained:

$$A_{S_C} = \int_{S_C} x_2 \, \mathrm{d}x_1 = \int_{-1}^{1} \left(\sum_{i=1}^{5} x_2^{(i)} \psi_i \right) \left(\sum_{j=1}^{5} x_1^{(j)} \frac{\mathrm{d}\psi_j}{\mathrm{d}\varepsilon} \right) \mathrm{d}\varepsilon \tag{57}$$

where $\psi_i, i = 1, 2, \ldots, 5$ are the interpolation functions in the fourth-order element.

The values of $x_2^{(i)}$ do not depend on ε and can be taken out of the integrals, yielding

$$A_{S_C} = \sum_{i=1}^{5} x_2^{(i)} \int_{-1}^{1} \psi_i \left(\sum_{j=1}^{5} x_1^{(j)} \frac{\mathrm{d}\psi_j}{\mathrm{d}\varepsilon} \right) \mathrm{d}\varepsilon \tag{58}$$

Since A_{S_C} has already been calculated using (56), the value of the mass conservative, smoothed coordinate $x_2^{(3)}$ expressed in terms of the coordinates of the surrounding points and $x_1^{(3)}$ can be calculated as

$$x_2^{(3)} = \frac{A_{S_C} - \sum_{i=1 i\neq 3}^{5} x_2^{(i)} \int_{-1}^{1} \psi_i \left(\sum_{j=1}^{5} x_1^{(j)} (\mathrm{d}\psi_j/\mathrm{d}\varepsilon) \right) \mathrm{d}\varepsilon}{\int_{-1}^{1} \psi_3 \left(\sum_{j=1}^{5} x_1^{(j)} (\mathrm{d}\psi_j/\mathrm{d}\varepsilon) \right) \mathrm{d}\varepsilon} \tag{59}$$

The developed smoothing algorithm is based on the conservation of the area enclosed by the drop contour, implying conservation of mass in the present case of two-dimensional incompressible flows. Previous proposed smoothing algorithms were found to cause significant variations in the drop area during the simulation period. In the results reported in this study, the area of the drop changes only slightly as the simulation progresses, keeping within 1% of its initial value throughout the simulation span. In this manner, it is assured that the analysis and conclusions presented here are not affected by mass losses. The observed small difference on the drop mass is due to the numerical integration procedure used in the time advancement of the surface nodes, and other possible numerical errors.

5.2. Surface remeshing

After a certain number of time steps during the evolution, the drops node distribution on a drop surface can become too clustered on certain sectors while becoming too dispersed on others; also high deformation can increase the perimeter causing the initial number of nodes to be insufficient for the new configuration. Both conditions negatively affect the numerical behaviour of the system of equations. A good practice is to remesh the surface of the drop every 3–10 time steps depending on the value of the capillary number.

DOI: 10.1002/fld

In order to obtain a two-dimensional algorithm capable of remeshing the deformed drop geometry, a closed Bézier curve is used, see [34],

$$C(t)=\sum_{i=0}^{N} P_i B_{i,N}(t) \tag{60}$$

where

$$B_{i,N}(t)=\binom{N}{i} t^i (1-t)^{N-1} \tag{61}$$

P_i are $N+1$ poles, and $0<t<1$ is a parameter. Given the fact that a Bézier curve yields only an approximation of a given geometry the node coordinates cannot be used as poles; therefore, an inversion process must be conducted such that

$$C(t)|_{t=t_i}=x_j^{(i)} \tag{62}$$

where $x_j^{(i)}$ is the jth coordinate of the node $x^{(i)}$. From (62) a linear system of equations is obtained yielding the values of poles that assure that the resulting Bézier curve passes through each of the nodes.

After the values of the poles are obtained, the perimeter of the geometry is integrated using this representation. By knowing the perimeter of the deformed surface, new nodes are placed at predetermined equally spaced distances along the boundary using the same integration scheme.

The number of initial boundary nodes is chosen in order to correctly represent the geometry without an unnecessary increase in the computational cost. In this study, 60 nodes (30 quadratic boundary elements) were chosen after having tested various discretizations, namely 30, 50 and 100 nodes, finding that 60 nodes had the best balance between approximation of the geometry and computational expense. For instance, the integration of the initial circular drop perimeter with 60 surface nodes and using 16 Gaussian integration points for each quadratic boundary element, results in a total error smaller than 0.0002%. It is worth noting, however, that this is only the initial number of points at the drop surface. In the numerical results, as the drop deforms its perimeter increases and the number of surface points is incremented up to approximately 120 nodes (60 quadratic boundary elements) trying to maintain a constant element length. In addition to the surface nodes, 30 collocation points inside each drop, initially uniformly distributed, are used in the DRM approximation of the extra stress tensor.

The proposed remeshing algorithm is valid for any type of drop deformation and flow configuration, outside the breakup condition, due to the used pole inversion algorithm, which assures that the resulting spline will necessarily pass through all the boundary nodes. A point of caution must be taken when the deformation of the drop is too extreme, which could require a denser node distribution in the vicinity of the irregularities to assure a good fit between the spline and the actual drop boundary.

6. RESULTS AND DISCUSSION

In this section, we will consider the motion caused by the interaction between the two initially circular drops, which are originally located one above the other and with the line joining their

DOI: 10.1002/fld

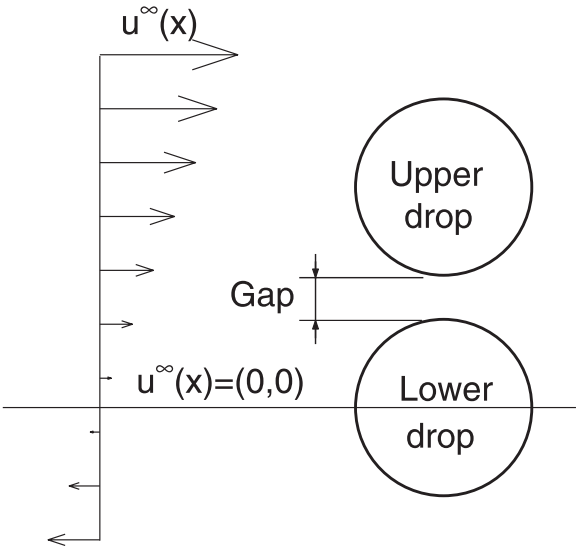

Figure 2. Initial set up of drops.

centres perpendicular to the streamlines of a linear shear flow. Particular attention to the trajectories of their mass centres as the interaction process evolves (mobility) is given. The initial set-up of the drops is presented in Figure 2, along with drop location relative to the shear flow. The figure shows that the lower drop is located along a streamline with zero velocity. This means that in the absence of other drops, the mass centre of the drop should remain static and the only effect of the base shear flow is to deform the initial shape. As it will be shown later, the presence of a second drop alters the zero velocity condition of the lower drop mass centre, moving the mass centres of both drops from their original transversal position, where the transversal direction is considered to be perpendicular to the direction of motion of the imposed linear shear flow. This transversal displacement is hereafter referred to as mobility. Simulations reported here have the following values of the non-dimensional parameters: $\dot{\gamma}_0 = 1.0$, $0.5 \leqslant \lambda^{NN} \leqslant 5$, $1 \leqslant Ca \leqslant 5$ and $n = 1.0, 0.8$ and 0.6, covering the range of some common polymer blends, see [11].

For illustrative purposes, let us first consider a particular case of an initial set-up corresponding to a transversal separation between the two drops of gap $= 0.5$ in the case when $\lambda^{NN} = 5$ and $Ca = 3$. Figure 3 shows the relative positions and deformation of the drops at different instants in time; the solid horizontal lines represent the original transversal position of the drop centres. As time progresses it becomes clear that the transversal distance between the two mass centres has decreased, and the position of each drop changes significantly from the initial conditions.

Here it is important to note that under the given linear shear flow condition and initial drops configuration, the behaviour of the drops transversal displacement is symmetric. This implies that the lower drop moves in the opposite transversal direction of the upper drop transversal motion but with the same magnitude. Therefore, for simplicity in the presentation, the remainder of this paper will focus on the motion of only the lower drop. As for the initial gap size between the two drops, large separations tend to lessen drop interactions, making the analysis in such cases difficult, given the small value of the cross flow motion of drop centres. On the other hand, very

DOI: 10.1002/fld

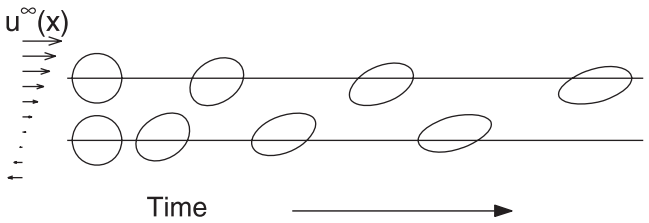

Figure 3. Time sequence in the interaction of two drops at gap = 0.5, $\lambda^{NN} = 5$, $Ca = 3$ and $n = 1.0$ for $t = 0.0$, $0.3\bar{3}$, $0.\bar{6}6$, 1.0.

small gap sizes tend to show numerical difficulties associated with very small surface separations [4]. A gap = 0.5 showed good magnitudes in the cross flow motion for the cases under study, while at the same time maintaining sufficient separation between drop surfaces to avoid numerical coalescence during the simulation time.

6.1. Effect of the viscosity ratio and the effective viscosity ratio

The power law index n has a strong influence on the behaviour of the system by altering the local value of the effective viscosity ratio inside the drop, i.e.

$$\lambda_{\text{eff}}(x) = \frac{\eta(\dot{\gamma}(x))}{\mu_e}$$

Shear thinning reduces the drop viscosity in regions of high deformation and consequently the value of λ_{eff}, which in turn reduces the strength of the interaction between the two drops (see Figure 4(A)). For the simulation period reported in the figure, the centre of the Newtonian drop, $n = 1.0$, reaches a maximum transversal displacement of 0.29, at this time the shear thinning drop with $n = 0.8$ only achieves 95% of the Newtonian displacement and the drop with $n = 0.6$ nearly completes 85%.

By displacing the lower drop from the zero velocity streamline, the longitudinal position (in the direction of the imposed shear flow) of the drop centre is also altered (Figure 4(B)). Positive displacements as those in Figure 4(A) cause the drop to move into the region of positive velocity streamlines, thus displacing it in the longitudinal positive direction. The effect of shear thinning in the longitudinal displacement is similar to its effect on the transversal displacements, increasing the separation of the drops as n decreases (Figure 4(B)).

It is interesting to see how the drop centre horizontal displacement in Figure 4(B) has an approximately linear growth after $t = 0.3$, corresponding to almost zero horizontal acceleration. By evaluating the slopes of these graphs it is possible to determine the corresponding drop centre horizontal velocity, as shown in the three top curves of Figure 5. It is important to observe that this case corresponds to a value of $\lambda^{NN} = 5$, i.e. a low value of the external fluid viscosity, corresponds to a case of low resistance by the external fluid to the drop longitudinal translation. Therefore, the significantly larger horizontal velocity achieved during the beginning of the interaction process, $t \leqslant 0.3$ is only slightly affected by the external fluid (see Figure 5). Figure 5 (three bottom curves), also displays the magnitude of the base flow velocity at the corresponding position of the drop centre during its transversal displacement in the time period $0 \leqslant t \leqslant 0.6$, which magnitude is continuously increasing. As can be observed from Figure 4(A), after $t = 0.6$ the drop is still moving in the positive

DOI: 10.1002/fld

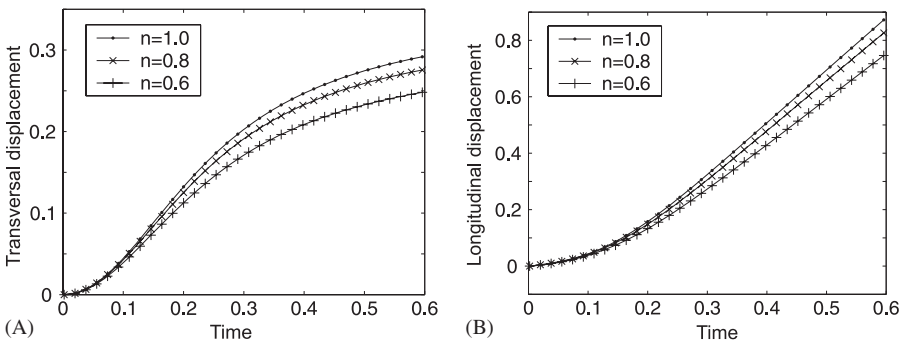

Figure 4. Displacement of shear thinning drop mass centres for $\lambda^{NN}=5$, $Ca=5$: (A) transversal and (B) longitudinal.

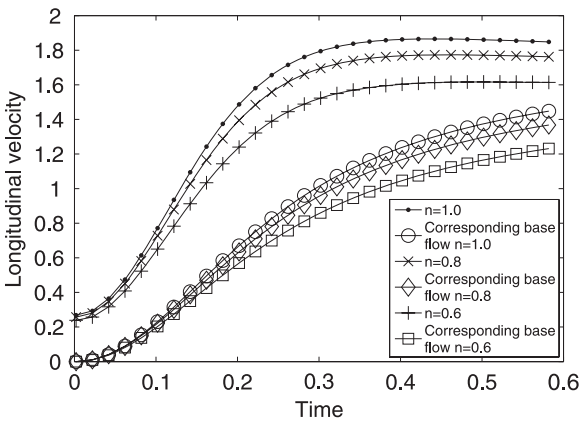

Figure 5. Longitudinal velocity of lower drop mass centre for $\lambda^{NN}=5$ and $Ca=5$ (three top curves), as well as the magnitude of the base flow velocity at the corresponding transversal position of the drop centre (bottom three curves).

transversal direction without a significant change on its longitudinal velocity (see Figure 5). As the drop is displaced transversally, its centre attains regions of higher base flow velocity. In this way the two set of curves in Figure 5 will tend to merge asymptotically, i.e. when the effect that one drop exerts on the other ceases, and the drop achieves its steady-state constant translational velocity.

It is also observed that stronger drop deformations than those of a Newtonian drop, $n=1$, are achieved by drops with $n<1$, see Figure 6. The drop deformation continues through the simulation period, where non-Newtonian drops become more slender as n decreases. This last effect, could induce breakup of non-Newtonian drops faster than in Newtonian drops by inducing capillary instabilities in the drop surface, after achieving sufficient drop deformation, thus favouring fluid mixing.

Similar drop behaviours to those given above are observed for a value of $\lambda^{NN}=3$ instead of 5. In Figure 7(A) and (B), a comparison between the obtained results for this value of λ^{NN} and two

DOI: 10.1002/fld

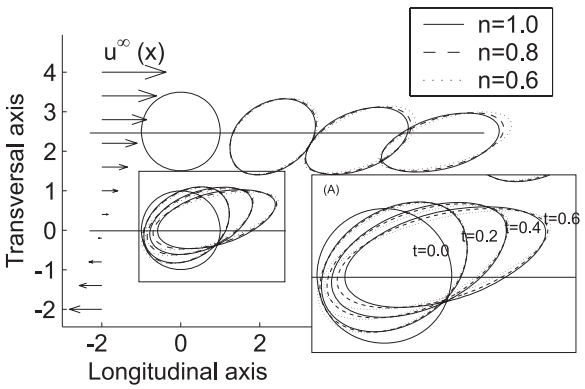

Figure 6. Shapes and positions of shear thinning drop for $\lambda^{NN}=5$, $Ca=5$.

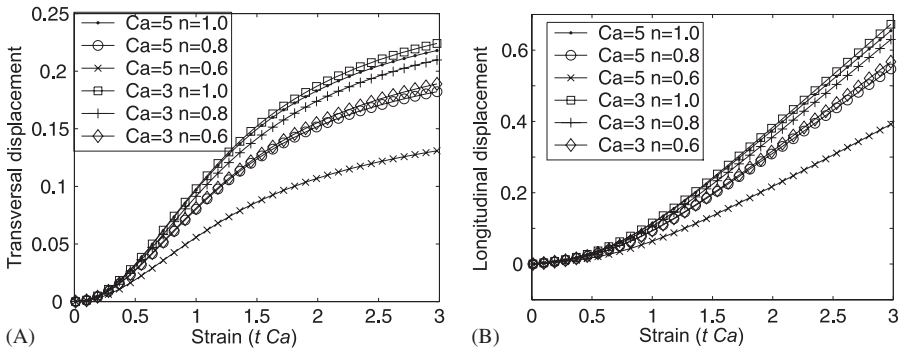

Figure 7. Displacement of shear thinning drop mass centres for $\lambda^{NN}=3$: (A) transversal and (B) longitudinal.

different values of $Ca=5$ and 3 are presented. As can be observed, lower values of the transversal displacements are achieved by drops with higher values of Ca, i.e. smaller values of the surface tension. On the other hand, stronger effect of the power law index n on the transversal displacement is observed for higher values of Ca. In the case of $Ca=3$, the maximum observed transversal displacement of the drop with $n=0.6$ is approximately 86% of that of the corresponding Newtonian drop, whereas for $Ca=5$ and $n=0.6$ the non-Newtonian drop achieves only 60% of the Newtonian drop displacement.

The longitudinal displacements in Figure 7(B) reflect the transversal displacement attained by the different drops, showing significant differences between shear thinning and Newtonian drops. By looking at the displacement of the mass centers in both directions (Figure 7) it can be observed that the trajectory of the drop with $Ca=5$ and $n=0.8$ is practically equal to the one with $Ca=3$ and $n=0.6$. The reason for this is that the reduction in λ_{eff} caused by the power law index in the second case is compensated by the lower value of the surface tension, i.e. higher values of Ca, in the first case inducing higher deformations. For higher value of Ca, the drop achieves higher deformation and therefore the effect of shear thinning for the same value of n is greater.

In Figure 7, the previously defined dimensionless time has been scaled with the capillary number (time $\times$ Ca), since in our dimensionless formulation of the problem the asymptotic velocity

DOI: 10.1002/fld

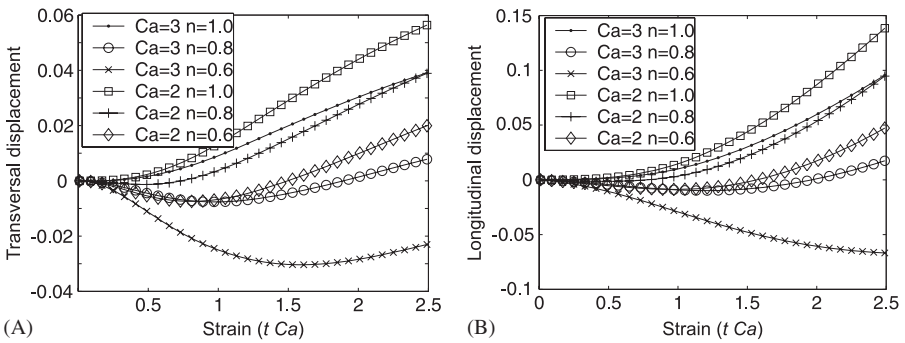

Figure 8. Displacement of shear thinning drop mass centres for $\lambda^{NN}=1$: (A) transversal and (B) longitudinal.

boundary condition (19) is linearly proportional to Ca. Therefore, comparison of displacement and velocities at different times using the original dimensionless time for different values of Ca results on shifted graphics; however, with the use of the modified time scale, time $\times Ca$, the corresponding graphics have the same origin of reference.

In the analysis presented for values of $\lambda^{NN}=3$ and 5, the behaviour of the drop evolution are similar; however, this is not the case when the value of $\lambda^{NN}\leqslant 1$. In Figure 8(A) and (B), we compare the resulting displacements, transversal and longitudinal, for two different values of $Ca=2$ and 3, when $\lambda^{NN}=1$. When $Ca=2$ and $n=0.8$ no motion is observed in the first few moments of the simulation and it is only after a significant reduction in the value of λ_{eff} that a reverse mobility is experienced by the drops, slightly pushing them apart.

This type of negative displacement was previously observed by Giraldo *et al.* [35] in cases of two Newtonian drops experiencing strong initial deformations. The negative displacement was caused by the fluid inside the lower drop moving away from a possible point of contact with the other drop as can be seen in Figure 9. This phenomenon increases with the increase in the initial drop deformations, as appears to be the case when $n=0.6$ and $Ca=3$. The reduction in the separation between the drops appears to create an increase in the drop surface tractions. This surface effect due to the reduction in separation, could be explainable through the lubrication theory and it is known to be of considerable influence in two-dimensional flows, see [4]. Given that, at some time during the simulation, the surfaces of the two drops could be in very close proximity, coalescence can be a possibility; however, this cannot be the case in this study since the required Van der Waals forces are not included, see [5].

A consequence of the negative transversal displacement is the change in the direction of the drop longitudinal motion, as shown in Figure 8(B). By displacing the lower drop in the negative transversal direction, its mass centre moves into the region where the imposed base flow has negative velocity, inducing the motion of the drop in the negative longitudinal direction. Owing to the symmetry of motion of the two drops (upper and lower), the upper drop reaches a streamline with a higher longitudinal velocity than the one it was originally in. Taking into account that the lower drop is moving in the opposite direction, and that the upper drop is moving faster it follows that, centre-to-centre distance increases at a higher rate than in the other cases considered, influencing drop dispersion.

DOI: 10.1002/fld

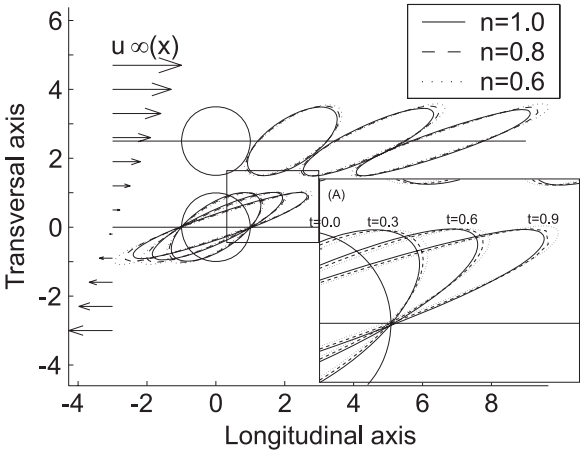

Figure 9. Shapes and positions of shear thinning drop for $\lambda^{NN}=1$.

The magnitudes of the obtained drop displacements for given values of *Ca* and viscosity ratio also requires some attention. Figures 7 and 8 show how the increase in *Ca*, i.e. reduction in surface tension, has the effect of reducing the transversal displacement of the drops due to the corresponding increase in the drop deformation. It is well known that the squeezing flow produces when two viscous drops approach each other is different to the one produced by the motion of two equivalent rigid particles. Because of the mobility of the fluid–fluid interface in the case of the drops, there is a slip velocity superposed on top of the flow motion between the drops, and the pressure build up is much less than that of the rigid particles (for more details, see [36]). Therefore, the behaviour of the interaction between the two drops depends on the amount of deformation experienced by them, with lower pressure build up between the drops as their deformation is higher. The above trend relating the magnitude of the translate displacement and the value of *Ca*, seems to be reversed in the cases when $n=0.6$, $Ca=2$ and 3, reported in Figure 8, where the case of $Ca=3$ shows a greater magnitude in the transversal displacement. However, it is important to observe that in this latter case the displacement occurs in the negative direction, i.e. in the region of reverse flow, in contrast with all the other cases considered before with positive displacement. It is also important to note that in this case the drop experiences a significant initial deformation due to its low value of *n* and large value of *Ca*. Due to the interaction of the drops, the fluid motion inside the drops tends to move the drop mass centre. In Figure 8, as the fluid moves towards the far end of the drop, the mass centre of the drop is displaced in the negative direction, explaining the larger negative displacements.

The motion of the lower drop in the negative transversal direction can also be observed in Figure 10 where the presence of negative transversal and longitudinal displacements of the lower drop centre, becomes more evident in the case when $\lambda^{NN}=0.5$, even for Newtonian drops, i.e. $n=1$, see Figure 10(A) and (B). As can be seen from these figures, once the upper drop moves a sufficient distance in the longitudinal direction, such that the distance between the two drop surfaces is large enough to reduce their initial mutual repulsion, the mobility phenomena start to take effect on the interaction process between the drops, moving the lower drop in the positive directions.

DOI: 10.1002/fld

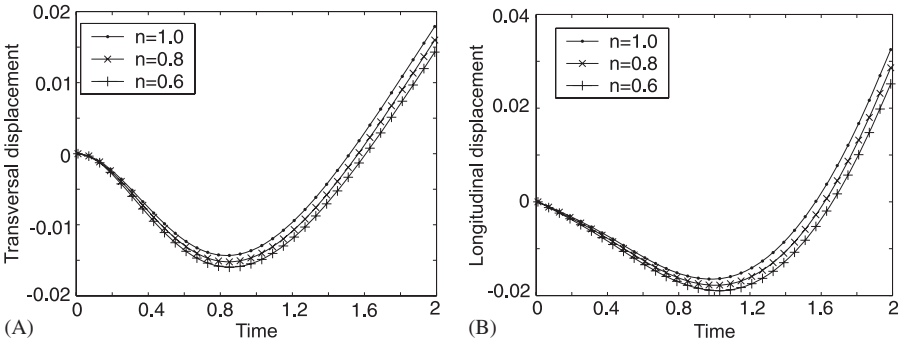

Figure 10. Displacement of shear thinning drop mass centres for $\lambda^{NN}=0.5$ and $Ca=1$: (A) transversal and (B) longitudinal.

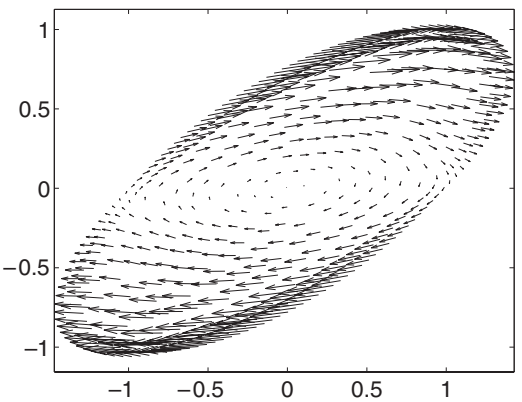

Figure 11. Internal velocity field for $\lambda^{NN}=0.5$ and $Ca=1$ (lower drop).

Figure 11 shows a plot of the internal velocity field at the lower drop in the case of $\lambda=0.5$, and $Ca=3$. It is important to point out that this velocity field corresponds to a drop that is simultaneously moving in both directions and at the same time deforming according to the imposed external flow field. In the figure, it is possible to observe the superposition effect of the translational motion and the drop internal recirculation. In the case of the upper drop, the internal recirculation appears to be hid by the large magnitude of the translational velocity.

So far the analyses have been made considering λ^{NN} constant and changing the values of Ca or n. Now, the focus will be set on a constant value of Ca and different values of λ^{NN} to understand how the intensity of the transversal motion and shear thinning is affected. Figure 12(A) shows the transversal displacements of the mass centres of a Newtonian ($n=1$) and a non-Newtonian drop ($n=0.6$) when $Ca=5$ (corresponding to small surface tension) and values of λ^{NN} ranging from 1 to 5. Newtonian displacements show that the magnitude of the transversal displacement is directly related to λ^{NN}, being greater for the larger values of this parameter. Results for $\lambda^{NN}=1$ and $n=1$ show a very small displacement from the initial position. In this case, the breaking point between mobility and separation is found somewhere below the value of $\lambda^{NN}=1$. For the given

DOI: 10.1002/fld

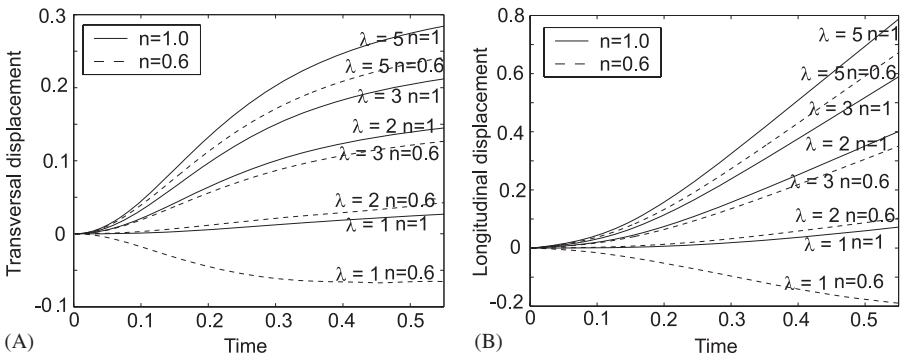

Figure 12. Displacement of shear thinning drop mass centres for $Ca=5$: (A) transversal and (B) longitudinal.

value of Ca, Newtonian drops always have bigger displacements than non-Newtonian drops with the important feature that for $\lambda^{NN}=1$ non-Newtonian drops experience negative displacements, which is not observed in the case of Newtonian drops. Longitudinal displacements (Figure 12(B)) show an even larger difference between the two extreme values of λ^{NN} than those of the transversal displacements.

In Figure 12(A), for $\lambda^{NN}=1$ and $n=0.6$, drop centre separation, i.e. negative transversal displacements, is obtained through out the simulation period achieving a constant negative value of the transversal displacement. In this manner, during the evolution process, the lower drop has been transversally positioned in a place that avoids any drop interaction that might cause mobility. For the value of $\lambda^{NN}=2$, the behaviour of the non-Newtonian drop is very similar to that of the Newtonian drop with $\lambda^{NN}=1$ and $n=1$, following almost the same transversal and longitudinal path showing that during the simulation period the value of λ_{eff} is approximately constant.

Finally, it is important to note that the difference between Newtonian and non-Newtonian drops is reduced as λ^{NN} increases. For instance, the maximum transversal displacement achieved during the simulation of the non-Newtonian drop with $\lambda^{NN}=2$ is approximately 29% of the corresponding displacement for a Newtonian drop, for $\lambda^{NN}=3$ it is approximately 57% and for $\lambda^{NN}=5$ almost 86%. The main cause for this reduction is that drop deformation is inhibited by higher values of λ^{NN}, reducing the value of $\dot{\gamma}$ in the interior of the drop. The effect of the reduction in the value of $\dot{\gamma}$ is more evident in Figure 13 for a value of $Ca=2$ (large surface tension), where for $\lambda^{NN}=3$ almost no difference is observed between the Newtonian and the non-Newtonian drops. The case of $\lambda^{NN}=5$ requires special attention, as the Newtonian and non-Newtonian drops have no difference whatsoever because the value of $\dot{\gamma}$ is below the value of $\dot{\gamma}_0$ at every point inside the drop, behaving as a Newtonian drop in accordance with the truncated power law model (see Section 2).

7. CONCLUSIONS

A direct boundary-only formulation for the simulation of the motion and deformation of non-Newtonian drops in Newtonian Stokes carrying flow was developed. The variation of the viscosity in the non-Newtonian fluid was modelled using the truncated power law and using an implicit velocity gradient calculation to obtain the corresponding shear stress. This approach constitutes

DOI: 10.1002/fld

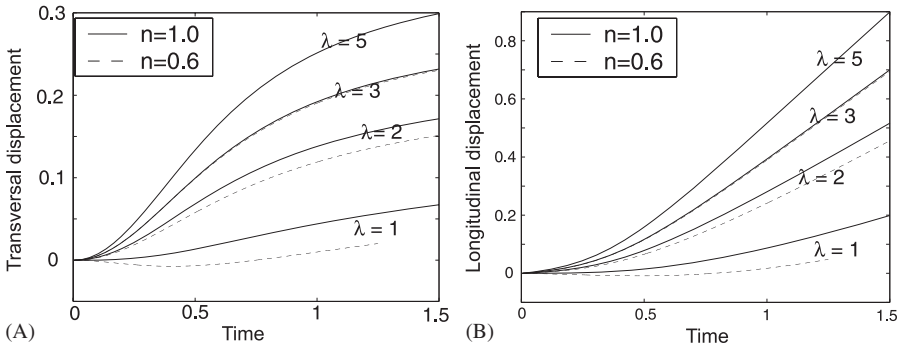

Figure 13. Displacement of shear thinning drop mass centres for $Ca=2$: (A) transversal and (B) longitudinal.

an efficient and physically accurate method for the simulation of drops interaction and deformation. Convergent solutions of the non-homogeneous and non-linear system of algebraic equations obtained after discretization of the corresponding system of integral equations was obtained using an iterative Newton–Raphson method with backtracking.

Under the conditions considered in this work, non-Newtonian effects were found to strongly influence the value of λ_{eff} in the domain interior to the drops, altering their behaviour in comparison with the corresponding Newtonian drop, with equal values of λ^{NN}. The difference between the behaviour of a non-Newtonian drop and an equivalent Newtonian drop is more significant as the value of the power index n is smaller than 1. The combination of Ca and λ^{NN} plays an important role in the intensity of the non-Newtonian behaviour, where high values of λ^{NN} show only limited divergence from the Newtonian behaviour, for most of the tested values of Ca. For values of $\lambda^{\text{NN}}=5$ and $Ca<2$ (large surface tension), the drops behave as Newtonian drops independent of the value of n, because the condition for shear-dependent viscosity ($\dot{\gamma}>\dot{\gamma}_0$) was not fulfilled. If the standard power law model is used instead of the proposed truncated model, shear thinning drops with values of $\lambda^{\text{NN}}=5, n<1.0$ and $Ca<2$ will exhibit shear thickening effects, which are not physically feasible.

Drops at constant viscosity ratio and different capillary numbers, presented two distinct behaviours. The first of them is what can be considered as a classical mobility, where the drops are pulled together in the transversal direction; in the second behaviour, a short range repulsion is observed, which appears to be caused by lubrication forces that increases the transversal distance and consequently increases the velocity at which drop centres separate. This separation was observed for Newtonian drops only for values of $\lambda^{\text{NN}}<1$, but can be induced by shear thinning for cases outside this condition if the deformation of the drop is high enough to reduce the value of λ_{eff} sufficiently.

APPENDIX A: EXPLICIT CALCULATION OF THE PSEUDO BODY FORCE TERMS

The selected iterative solution scheme requires the value of the pseudo-body forces in each of the collocation points obtained from the velocity fields found at the previous iteration (see Section 4). In this section the procedure to calculate this term is explained.

DOI: 10.1002/fld

The second invariant of the deformation tensor (4) can be expressed as

$$\dot{\gamma}=\sqrt{2(\varepsilon_{11}^2+2\varepsilon_{12}^2+\varepsilon_{22}^2)} \tag{A1}$$

where

$$\varepsilon_{11}=\frac{\partial u_1}{\partial x_1},\quad \varepsilon_{12}=\varepsilon_{21}=\frac{1}{2}\left(\frac{\partial u_1}{\partial x_2}+\frac{\partial u_2}{\partial x_1}\right),\quad \varepsilon_{22}=\frac{\partial u_2}{\partial x_2} \tag{A2}$$

From the continuity equation (1a) $\partial u_1/\partial x_1=-\partial u_2/\partial x_2$, therefore

$$\dot{\gamma}=\sqrt{2\left(2\left(\frac{\partial u_1}{\partial x_1}\right)^2+\frac{1}{2}\left(\frac{\partial u_1}{\partial x_2}+\frac{\partial u_2}{\partial x_1}\right)^2\right)} \tag{A3}$$

Using the definition of the extra stress tensor (16), expression (A3) and representing the velocity derivatives by (44), the following expression is obtained:

$$(\tau_{ij}^e)^{(t)}=[\lambda^{\mathrm{NN}}\Phi^{n-1}-\lambda^{\mathrm{N}}]\times\left(\frac{\partial F}{\partial x_j}F^{-1}u_i^{(t)}+\frac{\partial F}{\partial x_i}F^{-1}u_j^{(t)}\right) \tag{A4}$$

where

$$\Phi=\frac{\sqrt{\left(\frac{\partial F}{\partial x_1}F^{-1}u_1^{(t)}\right)^2+\frac{1}{2}\left(\frac{\partial F}{\partial x_2}F^{-1}u_1^{(t)}+\frac{\partial F}{\partial x_1}F^{-1}u_2^{(t)}\right)^2}}{\dot{\gamma}_0} \tag{A5}$$

Following a similar procedure for the derivatives of τ_{ij}^e than the one in (44) for the gradient of u_i, the divergence of the extra stress tensor can be expressed as

$$\frac{\partial\tau_{ij}^{e(t)}}{\partial x_j}=\frac{\partial F}{\partial x_j}F^{-1}[\lambda^{\mathrm{NN}}\Phi^{n-1}-\lambda^{\mathrm{N}}]\times\left(\frac{\partial F}{\partial x_j}F^{-1}u_i^{(t)}+\frac{\partial F}{\partial x_i}F^{-1}u_j^{(t)}\right) \tag{A6}$$

Relations (A4) and (A6) define the extra stress tensor and its divergence in terms of the nodal values of the velocity field inside a drop.

ACKNOWLEDGEMENTS

Mr M. Giraldo is supported in his PhD program by COLCIENCIAS under the Convocatoria de Doctorados Nacionales 2004.

REFERENCES

1. Rallison JM, Acrivos A. A numerical study of the deformation and burst of a viscous drop in an extensional flow. *Journal of Fluid Mechanics* 1978; **89**:191–200.
2. Power H. On the Rallison and Acrivos solution for the deformation and burst of viscous drops in an extensional flow. *Journal of Fluid Mechanics* 1987; **185**:547–550.
3. Primo ARM, Wrobel LC, Power H. Low Reynolds number deformation of viscous drops in a bounded flow region under surface tension. *Mathematical and Computer Modelling* 2000; **31**:99–118.

DOI: 10.1002/fld

4. Charles R, Pozrikidis C. Significance of the dispersed-phase viscosity on the simple shear flow of suspensions of two-dimensional liquid drops. *Journal of Fluid Mechanics* 1998; **365**:205–234.
5. Loewenberg M, Hinch EJ. Collision of two deformable drops in shear flow. *Journal of Fluid Mechanics* 1997; **338**:299–315.
6. Chen LS, Keh HJ. Hydrodynamic interactions of two freely suspended droplets in linear flow fields. *Journal of Colloid and Interface Science* 1998; **204**:66–76.
7. Khayat RE, Huneault MA, Utracki LA, Duquette R. A boundary element analysis of planar drop deformation in the screw channel of a mixing extruder. *Engineering Analysis with Boundary Elements* 1998; **21**:155–168.
8. Khayat RE, Luciani A, Utracki LA. Boundary-element analysis of planar drop deformation in confined flow. Part 1. Newtonian fluids. *Engineering Analysis with Boundary Elements* 1997; **19**:279–289.
9. Khayat RE, Luciani A, Utracki LA, Godbille F, Picot J. Influence of shear and elongation on drop deformation in convergent–divergent flows. *International Journal of Multiphase Flow* 2000; **26**:17–44.
10. Briscoe BJ, Lawrence CJ, Mietus WGP. A review of immiscible fluid mixing. *Advances in Colloid and Interface Science* 1999; **81**:1–17.
11. Kim SJ, Han CD. Finite element analysis of axisymmetric creeping motion of a deformable non-Newtonian drop in the entrance region of a cylindrical tube. *Journal of Rheology* 2001; **45**(6):1279–1303.
12. Favelukis M, Lavrenteva OM, Nir A. Deformation and breakup of a non-Newtonian slender drop in an extensional flow. *Journal of Non-Newtonian Fluid Mechanics* 2005; **125**:49–59.
13. Yuan X-F, Doi M. A general approach for modelling complex fluids: its application to concentrated emulsions under shear. *Colloids and Surfaces A*: *Physicochemical and Engineering Aspects* 1998; **144**:305–318.
14. Kim SJ, Kim S, Kwon Y. Deformation of multiple non-Newtonian drops in the entrance region. *Korea–Australia Rheology Journal* 2003; **15**(2):75–82.
15. Lorentz HA. A general theorem concerning the motion of a viscous fluid and a few consequences derived from it. *Verslag der Koninklijke Akadamie van Wetenschappen te Amsterdam* 1896; **5**:168–174.
16. Youngren GK, Acrivos A. A stokes flow past a particle of arbitrary shape: a numerical method of solution. *Journal of Fluid Mechanics* 1975; **69**(2):377–403.
17. Brebbia CA, Dominguez J. *Boundary Elements*: *An Introductory Course* (2nd edn). Computational Mechanics Publications: Southampton, 1992.
18. Khayat RE. A boundary-only approach to the deformation of a shear-thinning drop in extensional Newtonian flow. *International Journal for Numerical Methods in Fluids* 2000; **33**:559–581.
19. Toose EM, Geurts BJ, Kuerten JGM. A boundary integral method for two-dimensional (non)-Newtonian drops in slow viscous flow. *Journal of Non-Newtonian Fluid Mechanics* 1995; **60**:129–154.
20. Khayat RE, Derdouri A, Frayce D. Boundary-element analysis of three dimensional transient mixing processes of newtonian and viscoelastic fluids. *International Journal for Numerical Methods in Fluids* 1998; **28**:815.
21. Greco F. Drop deformation for non-Newtonian fluids in slow flows. *Journal of Non-Newtonian Fluid Mechanics* 2002; **107**:111–131.
22. Byron Bird R, Armstrong RC, Hassager O. *Dynamics of Polymeric Liquids*, *Volume 1*, *Fluid Mechanics* (2nd edn). Wiley: New York, 1987.
23. Favelukis M, Albalak RJ. Bubble growth in viscous Newtonian and non-Newtonian liquids. *The Chemical Engineering Journal* 1996; **63**:149–155.
24. Partridge P, Brebbia CA, Wrobel LC. *The Dual Reciprocity Boundary Element Method*. Computational Mechanics Publications: Southampton, 1992.
25. Chen CS, Brebbia CA, Power H. Dual reciprocity method using compactly supported radial basis functions. *Communications in Numerical Methods in Engineering* 1999; **15**:137–150.
26. Portapila M, Power H. Iterative solution schemes for quadratic DRM-MD. *Numerical Methods for Partial Differential Equations* 2008; accepted (published online 18 March 2008).
27. Flórez WF, Power H. Multi-domain dual reciprocity for the solution of inelastic non-Newtonian problems. *Computational Mechanics* 2001; **27**:396–411.
28. Power H, Botte V. An indirect boundary element method for solving low Reynolds number Navier–Stokes equations in a three-dimensional cavity. *International Journal for Numerical Methods in Engineering* 1998; **41**:1485–1505.
29. Florez W, Power H, Chejne F. Multi-domain dual reciprocity BEM approach for the Navier–Stokes system of equations. *Communications in Numerical Methods in Engineering* 2000; **16**:671–681.
30. Giraldo M, Power H, Flórez WF. Evaluation of strong shear thinning non-Newtonian fluid flow using single domain DR-BEM. In *Boundary Elements and Other Mesh Reduction Methods XXIX*, Brebbia CA, Poljak D, Popov V (eds). WIT Press: Southampton, 2007; 111–120.

DOI: 10.1002/fld

31. Henao CA. *Simulación y Evaluación de Proceso Químicos*. Universidad Pontificia Bolivariana: Medellín, 2005.
32. Telles J. A self-adaptative coordinate transformation for efficient numerical evaluation of general boundary element integrals. *International Journal for Numerical Methods in Engineering* 1987; **24**:959–973.
33. Cristini V, Blawzdziewicz J, Loewenberg M. An adaptive mesh algorithm for evolving surfaces simulations of drop breakup and coalescence. *Journal of Computational Physics* 2001; **168**:445–463.
34. Bartels RH, Beatty JC, Barsky BA. *An Introduction to Splines for Use in Computer Graphics and Geometric Modelling*. Morgan Kaufmann: San Francisco, CA, 1998.
35. Giraldo M, Power H, Flórez WF. Mobility of a viscous Newtonian drop in shear Newtonian flow. *International Journal of Dynamics of Fluids* 2008; accepted.
36. Kim S, Karrila SJ. *Microhydrodynamics*. Butterworth-Heinemann: Boston, MA, 1991.

DOI: 10.1002/fld